Chemical Science

ROYAL SOCIETY OF CHEMISTRY

EDGE ARTICLE

View Article Online
View Journal | View Issue

Cite this: *Chem. Sci.*, 2021, **12**, 2231

All publication charges for this article have been paid for by the Royal Society of Chemistry

Activation of ammonia and hydrazine by electron rich Fe(II) complexes supported by a dianionic pentadentate ligand platform through a common terminal Fe(III) amido intermediate†‡

Lucie Nurdin,[a] Yan Yang,[b] Peter G. N. Neate,[c] Warren E. Piers, *[a] Laurent Maron, *[b] Michael L. Neidig,*[c] Jian-Bin Lin[a] and Benjamin S. Gelfand [a]

We report the use of electron rich iron complexes supported by a dianionic diborate pentadentate ligand system, **B_2Pz_4Py**, for the coordination and activation of ammonia (NH_3) and hydrazine (NH_2NH_2). For ammonia, coordination to neutral (B_2Pz_4Py)Fe(II) or cationic $[(B_2Pz_4Py)Fe(III)]^+$ platforms leads to well characterized ammine complexes from which hydrogen atoms or protons can be removed to generate, fleetingly, a proposed (B_2Pz_4Py)Fe(III)–NH_2 complex (**3_{Ar}-NH_2**). DFT computations suggest a high degree of spin density on the amido ligand, giving it significant aminyl radical character. It rapidly traps the H atom abstracting agent 2,4,6-tri-*tert*-butylphenoxy radical (ArO$^\bullet$) to form a C–N bond in a fully characterized product (**2_{Ar}**), or scavenges hydrogen atoms to return to the ammonia complex (B_2Pz_4Py)Fe(II)–NH_3 (**1_{Ar}-NH_3**). Interestingly, when (B_2Pz_4Py)Fe(II) is reacted with NH_2NH_2, a hydrazine bridged dimer, (B_2Pz_4Py)Fe(II)–NH_2NH_2–Fe(II)(B_2Pz_4Py) (**$(1_{Ar})_2$-NH_2NH_2**), is observed at −78 °C and converts to a fully characterized bridging diazene complex, **4_{Ar}**, along with ammonia adduct **1_{Ar}-NH_3** as it is allowed to warm to room temperature. Experimental and computational evidence is presented to suggest that (B_2Pz_4Py)Fe(II) induces reductive cleavage of the N–N bond in hydrazine to produce the Fe(III)–NH_2 complex **3_{Ar}-NH_2**, which abstracts H$^\bullet$ atoms from **$(1_{Ar})_2$-NH_2NH_2** to generate the observed products. All of these transformations are relevant to proposed steps in the ammonia oxidation reaction, an important process for the use of nitrogen-based fuels enabled by abundant first row transition metals.

Received 24th November 2020
Accepted 21st December 2020

DOI: 10.1039/d0sc06466a

rsc.li/chemical-science

Introduction

Storing energy in chemical bonds, in particular protons and electrons in nitrogen-based fuels, has become an attractive alternative to supply carbon-free energy carriers on-demand.[1,2] Ammonia (NH_3) has recently emerged as a promising candidate for carbon-free fuel replacements[3] because it is prepared on an industrial scale through the well-established Haber–Bosch (H–B) process, and the infrastructure to store and distribute this chemical are available worldwide.[4] With the increasing use of renewable sources to power the H–B process, and with the tremendous effort dedicated to using renewable hydrogen from water electrolysis as an alternative to steam reformation of methane, the potential for use of NH_3 as a less carbon-intensive fuel is rising.[5]

Ammonia can be used directly in NH_3 fuel cells through the ammonia oxidation reaction (AO, Scheme 1), or can be used as a medium to store hydrogen (H_2) resulting from its high energy density.[6] However, to mediate this transformation under manageable conditions and reasonable rates and selectivities, catalysts are required. While there have been several reports on heterogeneous catalysts for ammonia oxidation with limited success,[7] examples of homogeneous catalysts are attracting increasing attention.[8–12] Homogeneous catalysts offer the prospect of greater selectivity, more control over active site steric and electronic properties, and an opportunity to understand the fundamental chemistry involved through detailed spectroscopic and structural studies.[13]

The oxidation of NH_3 into N_2 is an inherently challenging process due to the difficulty in breaking all three of its strong N–H bonds (the first N–H bond dissociation energy, BDE, of

[a]*Department of Chemistry, University of Calgary, 2500 University Drive NW, Calgary, Alberta, T2N 1N4, Canada. E-mail: wpiers@ucalgary.ca*

[b]*LPCNO, Université de Toulouse, INSA, UPS, Toulouse, France*

[c]*Department of Chemistry, University of Rochester, Rochester, New York 14627, USA*

† The authors would like to dedicate this manuscript to Prof. Robert H. Morris, University of Toronto, scholar, gentleman and organometallic chemist extraordinaire.

‡ Electronic supplementary information (ESI) available: Experimental and characterization details for all new compounds, including spectroscopic data, X-ray crystallographic data and computational details with the cartesian coordinates for calculated structures. CCDC codes 2044409–2044414 contain the crystallographic data for compounds **1_{Tol}-NH_3**, **2_{Tol}**, **3_{Tol}-NH_3^+**, **3_{Tol}-Br**, **3_{Tol}-F**, and **4_{Tol}**, respectively. For ESI and crystallographic data in CIF or other electronic format see DOI: 10.1039/d0sc06466a

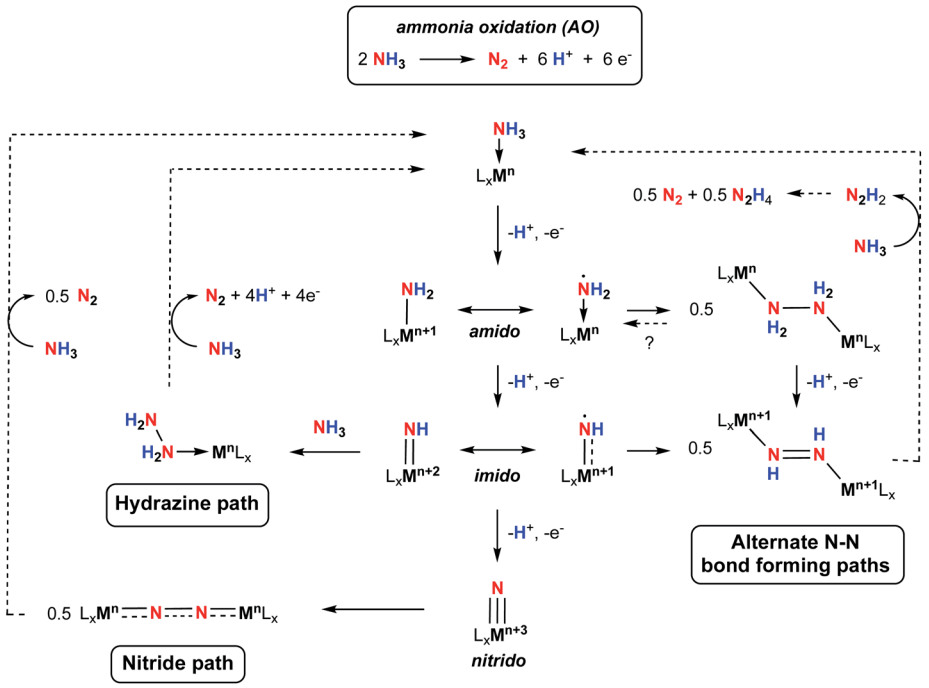

Scheme 1 Postulated steps and intermediates in homogeneous ammonia oxidation.

NH_3 is 107.6 kcal mol^{-1}),[14] as well as the multiple electron and proton transfers involved in the formation of N_2 (Scheme 1).[15] The energy associated with N–H bond breaking can be lowered by coordination of NH_3 to a metal center, and subsequent strategies such as N–H oxidative addition,[16] heterolytic cleavage through metal–ligand cooperativity,[17–21] or hydrogen atom abstraction (HAA)[8,9,22–27] have been successful at mediating N–H bond cleavage of NH_3. In addition to N–H bond cleavage, N–N bond formation is a key process. Initially, two classes of N–N bond formation were postulated by analogy to water oxidation mechanisms, namely nucleophilic attach by NH_3 on electrophilic imido groups (the "hydrazine path", Scheme 1), or direct homocoupling of two terminal nitride intermediates (the "nitride path", Scheme 1).[10] While the nitride pathway requires a +3 change in the metal oxidation state to yield metal–nitride complexes, which can then undergo N–N homocoupling, the hydrazine pathway only requires a +2 change in the metal oxidation state to yield a metal–imido complex, which can then react further with NH_3 to form a hydrazine adduct *via* N–N coupling. More recently, N–N bond formation *via* coupling of other intermediates, for example M–NH_2 or M=NH compounds with significant spin density on the amido/imido nitrogen, have been proposed.[28] This path to N–N bond formation requires only a +1 oxidation state change and may be more important for catalysts based on first row transition metals. Thus, despite the recent interest in AO, much remains to be uncovered concerning the mechanistic nuances of this process. The key to advancing our understanding of the fundamental reactivity profiles and thermochemistry associated with the cleavage of the individual N–H bonds, the nature of intermediates involved in this transformation, and the character of N–N bond forming steps lies in detailed mechanistic investigations on a variety of systems.[23] Furthermore, to operate at scale, higher stability under typical catalytic conditions is required, as well as catalysts based on sustainable metals. Notably, only one catalyst featuring an earth-abundant, first-row transition metal has been reported but shows low TON due to catalyst decomposition.[11] There is therefore room for fundamental research in catalyst design and mechanistic studies to advance this nascent area of catalysis.

In terms of catalyst design, the supporting ligand must be robust enough to support the metal center in multiple oxidation states, in particular when using first-row transition metals. Polypyridyl ligands have been used in three out of the five reported homogeneous catalysts for AO.[9–11] These and related tetrapodal pentadentate platforms have been employed across the periodic table and have been successful at supporting a variety of metal centers in various oxidation states, mainly in the context of water oxidation/reduction catalysis.[29–33] Bullock and coworkers recently reported a detailed theoretical investigation using the **PY5** ligand platform[34,35] for AO with M = Cr, Mo, W, Mn, Fe, Ru, Os.[36] They observed that the **[PY5]Fe(II)** complex behaved quite differently to the rest of the metals investigated, notably due to the significant radical character of the Fe–amido and Fe–imido intermediates computed. We therefore thought of using our tetrapodal dianionic pentadentate $\mathbf{B_2Pz_4Py}$ ligand platform, which has been successful at accessing a variety of first-row metal complexes.[37–41] The $\mathbf{B_2Pz_4Py}$ ligand features two borate moieties at the linkage position between the four equatorial pyrazole arms and the axial pyridine, rendering the ligand dianionic and slightly more rigid than the **PY5** platform.[42] The charge modification from the **PY5**

to the $\mathbf{B_2Pz_4Py}$ platform renders complexes of M(II) ions neutral, and higher oxidation state complexes are generally more accessible with this more electron rich ligand system.[37] In addition, the decrease in the overall charge of the complex favors pathways involving dimerization due to lower coulombic repulsion.

Herein we report the synthesis and characterization of Fe complexes bearing the $\mathbf{B_2Pz_4Py}$ ligand platform and their reactivity with ammonia and hydrazine. The reactivity observed is supported by both experimental and theoretical mechanistic studies involving higher-valent, reactive intermediates. In particular, evidence for the involvement of a reactive terminal Fe(III)–NH_2 species is presented; as indicated in Scheme 1, such compounds are proposed to be key intermediates of AO but are rarely isolated and characterized[43–45] in the absence of Lewis acid stabilization.[46,47]

Results and discussion

We have previously reported two versions of the $\mathbf{[B_2Pz_4Py]HLi}$ ligand precursor, differing by the aromatic ring bound to the borate group (Ar = Ph,[39] *p*-Tol[37]). Our initial report on Fe was carried out using the phenyl version of the ligand, featuring complexes $\mathbf{1_{Ph}}$**-THF** and $\mathbf{1_{Ph}}$ (Scheme 2) but these derivatives were characterized by poor solubility in many solvents. Incorporation of tolyl groups leads to greatly enhanced solubility of the resulting Fe complexes, and the tolyl derivative was employed instead for the majority of the chemistry described herein. An improved synthesis was developed to make complexes $\mathbf{1_{Ar}}$**-THF** by treating the monolithium pyridinium salt directly with one equivalent of $Fe(HMDS)_2$ (ref. 48 and 49) in THF (Scheme 2). This synthesis allowed for a greater yield of LiBr free product, and simplification of the purification procedure. Compounds $\mathbf{1_{Ar}}$ are isolated as light green solids in ≈70% yield by heating $\mathbf{1_{Ar}}$**-THF** under vacuum for four hours (Scheme 2). While $\mathbf{1_{Ph}}$ is insoluble in aprotic solvents such as toluene or benzene, $\mathbf{1_{Tol}}$ is readily dissolved in these media. The difference in solubility between $\mathbf{1_{Ph}}$ and $\mathbf{1_{Tol}}$ is striking and can serve as a distinguishing feature for the isolation of various key complexes, under the assumption that the difference between the two Ar groups does not significantly influence the course of reactivity at the Fe center. Evans method measurement of the magnetic susceptibility of $\mathbf{1_{Tol}}$ gives a $\mu_{eff} = 4.99$, consistent with a high spin (HS) system with 4 unpaired electrons ($S = 2$) as previously reported for $\mathbf{1_{Ph}}$.[39] $\mathbf{1_{Ar}}$ can coordinate a variety of L type ligands, including THF and MeCN. While THF adducts $\mathbf{1_{Ar}}$**-THF** are HS, stronger π-acceptor ligands such as MeCN enforce a low spin (LS) environment ($S = 0$), noted by a characteristic ^{1}H NMR spectrum of a diamagnetic Fe(II) complex obtained in CD_3CN (Fig. S1 and S2‡). This is supported by the data obtained from Mössbauer spectroscopy. A solid sample of $\mathbf{1_{Tol}}$ gives an isomer shift consistent with a HS system ($\delta = 1.04$ mm s^{-1} and $\Delta E_Q = 0.93$ mm s^{-1}, Fig. S3‡). In contrast, when a pale green benzene solution of $\mathbf{1_{Tol}}$ under a dinitrogen atmosphere is frozen to 80 K, it turns orange and gives rise to a Mössbauer spectrum with parameters supporting a LS configuration ($\delta = 0.44$ mm s^{-1} and $\Delta E_Q = 0.43$ mm s^{-1} Fig. S4‡), suggesting coordination of dinitrogen and a spin state change. Complexes $\mathbf{1_{Ar}}$ and $\mathbf{1_{Ar}}$**-L** are extremely air sensitive and can easily be oxidized as shown by a low potential for the Fe(II/III) redox couple at −0.44 V *vs.* Fc/Fc^+ (Fig. S5‡). When exposed to O_2, Fe(II) complexes quickly react to form an iron μ-oxo bridge species, Fe(III)–O–Fe(III).[50] Therefore, all reactions must be performed under rigorously air free conditions.

Treatment of $\mathbf{1_{Ar}}$ with $^{14}NH_3$ (1 atm) results in a clear color change from light green to dark brown forming the NH_3 adduct $\mathbf{1_{Ar}}$**-^{14}NH$_3$** (Scheme 2). This is accompanied by a transition to a new ^{1}H NMR spectrum featuring peaks located in the diamagnetic region, although the resonances are quite broadened. When $^{15}NH_3$ is employed, the singlet at +2.73 ppm becomes a doublet with a $^1J_{15N-1H}$ of 62.4 Hz (Fig. S6‡), consistent with the other $^{15}NH_3$ adducts previously reported.[8,9,26] The ^{11}B chemical spectrum also changes drastically from +38.4 ppm for complex $\mathbf{1_{Tol}}$ to −1.6 ppm for $\mathbf{1_{Tol}}$**-^{n}NH$_3$**, which is in the region of diamagnetic metal complexes with this ligand platform.[40] $\mathbf{1_{Tol}}$**-^{n}NH$_3$** was isolated in 96% yield as a brown solid (Scheme 2) and was characterized by single-crystal X-ray crystallography (Fig. 1). The Fe–N10 bond of 2.072(2) Å confirms the LS configuration by comparison to similar LS Fe–NH_3 adducts.[11,44,51,52] In addition, the average bond length of 1.998 Å for the five other Fe–N bonds *vs.* 2.115 Å for $\mathbf{1_{Ph}}$**-THF** (HS)[39] also attests to the LS spin structure of this Fe(II)–NH_3 complex. The broadening of the chemical shifts in the ^{1}H NMR spectrum may be due to a fast spin flipping between the LS and HS systems.[53] Peters and coworkers recently reported that both LS and HS configurations of their polypyridyl Fe(II)–NH_3 complex were present in the solid-state structure.[11] DFT calculations on the ground state of $\mathbf{1_{Tol}}$**-NH$_3$** show that the LS and HS systems only differ by 5.6 kcal mol^{-1}. Furthermore, NH_3 has a field strength located between THF and MeCN, where THF is the weakest field ligand and MeCN the strongest.[54] The Mössbauer parameters of $\mathbf{1_{Tol}}$**-NH$_3$** ($\delta = 0.55$ mm s^{-1} and $\Delta E_Q = 0.22$ mm s^{-1}) also suggest that the LS configuration is favored at low temperatures, but some dissociation of the NH_3 ligand could not be prevented under an N_2 atmosphere and the

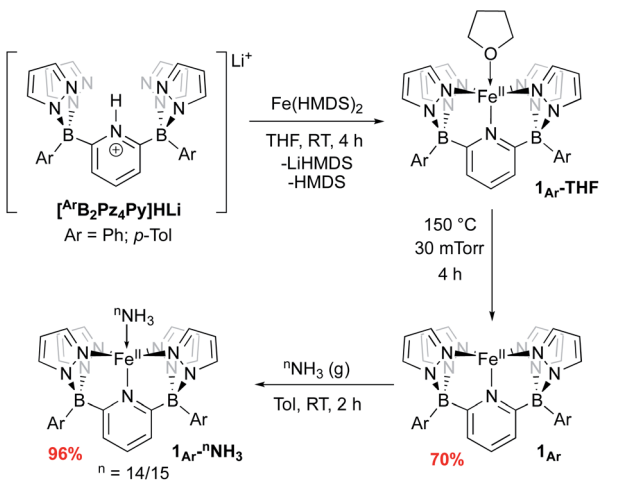

Scheme 2 Synthesis of $\mathbf{1_{Ar}}$ and $\mathbf{1_{Ar}}$-^{n}NH$_3$.

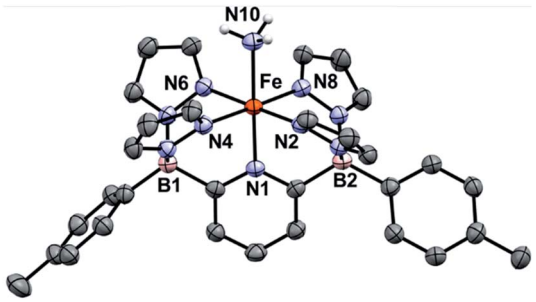

Fig. 1 ORTEP diagrams for $\mathbf{1_{Tol}}$-NH_3. Hydrogen, boron, carbon, nitrogen, and iron atoms are white, pink, grey, light blue, and orange respectively. Thermal ellipsoids are shown at the 50% probability level. Calculated hydrogen atoms are omitted for clarity except those on the ammonia ligand (N10). The solvent molecule has been omitted for clarity. Selected bond distances (Å): Fe–N1, 1.969(2); Fe–N2, 2.000(2); Fe–N4, 1.964(2); Fe–N6, 2.000(2); Fe–N8, 2.004(2); Fe–N10, 2.072(2). Selected bond angles (°): N1–Fe–N2, 91.1(1); N2–Fe–N4, 92.8(8); N1–Fe–N10, 179.0(9). Further metrical data are given in Table S1.‡

purported LS dinitrogen Fe(II) adduct is also present in the spectrum in variable amounts (≈20%) in these spectra (Fig. S7‡).

An important first step in AO is the loss of "H˙" from amine complexes, so reactions of $\mathbf{1_{Ar}}$-$^{n}\mathbf{NH_3}$ with hydrogen atom abstractors (HAAs) were explored. This strategy has been employed in a variety of systems,[22,27] and has been successful for catalytic and stoichiometric AO.[8,9] To choose a suitable reagent, the first N–H bond dissociation energy (BDE) of $\mathbf{1_{Tol}}$-$\mathbf{NH_3}$ was computed and found to be 75.5 kcal mol^{-1}, which is significantly lower than the first N–H BDE of NH_3 (107.6 kcal mol^{-1}).[14] No reaction was observed when TEMPO was used as the HAA (O–H = 70.0 kcal mol^{-1}),[14] so the stronger 2,4,6-tri-*tert*-butylphenoxy radical (ArO˙, BDE of ArO–H = 81.6 kcal mol^{-1}),[14] which has proven successful in mediating N–H bond cleavage,[8,26] was then tried. To deconvolute this chemistry, both the phenyl and tolyl ligands were employed, exploiting their differing solubility properties as described. Accordingly, treatment of $\mathbf{1_{Ph}}$-$^{15}\mathbf{NH_3}$ with excess ArO˙ for 16 h at room temperature in toluene, gave a new diamagnetic, forest green product, $\mathbf{2_{Ph}}$-$^{15}\mathbf{N}$ (Scheme 3). The ^{1}H NMR spectrum of the product features three key resonances: two different – ^{t}Bu groups in the alkyl region (1.64 and 0.83 ppm), and one deshielded doublet at +17.82 ppm (J = 66.6 Hz) integrating for 1H and suggesting a $^1J_{15N-1H}$ coupling (Fig. S8‡).[55] This doublet becomes a singlet when $\mathbf{1_{Ph}}$-$^{14}\mathbf{NH_3}$ is employed in the reaction, confirming the assignment as a ^{15}N–H proton (Fig. S9‡). The parameters obtained from the Mössbauer spectrum of this species are consistent with a low spin Fe(II) system (δ = 0.29 mm s^{-1} and ΔE_Q = 0.97 mm s^{-1}, Fig. S10‡). Unfortunately, due to the poor solubility of $\mathbf{2_{Ph}}$, no X-ray quality crystals could be obtained. The same reaction using $\mathbf{1_{Tol}}$-$^{n}\mathbf{NH_3}$ gave a spectroscopically similar product, but $\mathbf{2_{Tol}}$ could not be isolated from the ArOH by product of the reaction due to its greater solubility (Fig. S11‡). Luckily, a pentane solution of this reaction mixture stored in the glove box freezer deposited blue, X-ray quality crystals and the molecular structure of $\mathbf{2_{Tol}}$ was revealed (Fig. 2). This structure is fully consistent with all the spectroscopic and analytical data obtained for $\mathbf{2_{Ph}}$. Analysis of the metrical data confirmed the depiction of $\mathbf{2_{Ar}}$ as an Fe(II) activated imine complex. In particular, the short N10–C1, 1.330(4); C2–O, 1.240(5); C3–C4 1.353(6); and C5–C6 1.357(5) bond distances (Å) confirm the double bond assignment around the conjugated ring. Interestingly, the short Fe–N10 bond distance, 1.859(3) Å, attests to the stability of compounds $\mathbf{2_{Ar}}$, and when $\mathbf{2_{Ar}}$ is treated with excess ArO˙ and/or excess NH_3, no further reactivity is observed (Fig. S12‡). The stability of $\mathbf{2_{Ar}}$ is most likely enhanced due to the hydrogen bonding interaction between NH–O (2.145(4) Å), see Fig. 2.

Isolation of products $\mathbf{2_{Ar}}$ suggests that ArO˙ abstracts a hydrogen atom from $\mathbf{1_{Ar}}$-$\mathbf{NH_3}$ to form Fe(III)–NH_2 ($\mathbf{3_{Ar}}$-$\mathbf{NH_2}$) which then is trapped by excess aryloxy radical; the reaction does not proceed unless excess radical is employed. Consistent with this, signals for Ar–OH are observed in the crude reaction

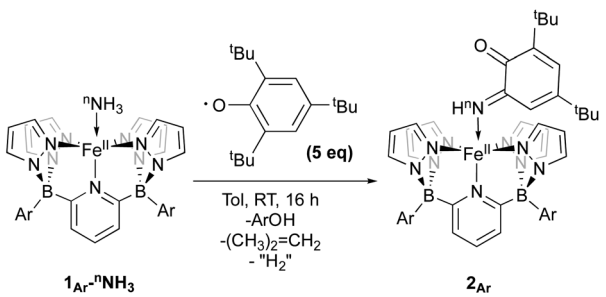

Scheme 3 Reactivity of $\mathbf{1_{Ar}}$-$^{n}\mathbf{NH_3}$ with ArO˙ to form $\mathbf{2_{Ar}}$.

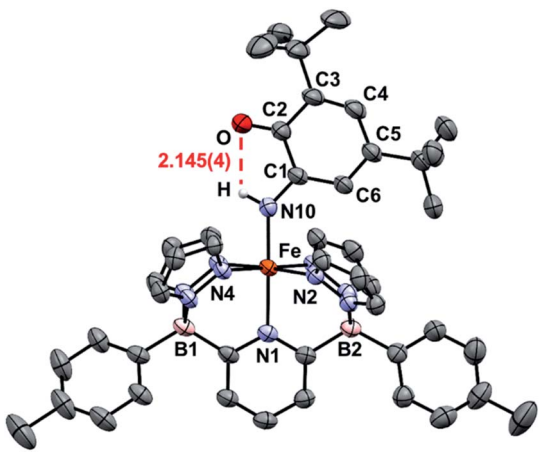

Fig. 2 ORTEP diagrams for $\mathbf{2_{Tol}}$. Hydrogen, boron, carbon, nitrogen, oxygen, and iron atoms are white, pink, grey, light blue, red, and orange respectively. Thermal ellipsoids are shown at the 50% probability level. Calculated hydrogen atoms are omitted for clarity except those on atom N10. The hydrogen bonding interaction is shown in red. Selected bond distances (Å): Fe–N1, 2.036(3); Fe–N2, 1.986(3); Fe–N4, 1.963(3); Fe–N10, 1.859(3); N10–C1, 1.330(4); C2–O, 1.240(5); C1–C2, 1.484(5); C2–C3, 1.477(5); C3–C4, 1.353(6); C4–C5, 1.437(6); C5–C6, 1.357(5); C6–C1, 1.429(5); O–H, 2.145(4). Selected bond angles (°): N1–Fe–N2, 91.6(1); N2–Fe–N4, 92.9(1); N1–Fe–N10, 178.1(1); Fe–N10–C1, 136.2(2). Further metrical data are given in Table S1.‡

mixture (Fig. S13‡). The loss of a ^{t}Bu group from the aryloxy framework implies that iso-butene is released, along with two hydrogen atoms; the former was detected by GC-MS in the headspace of the reaction (Fig. S14‡). Thevenet and coworkers reported similar reactivity with ArO$^{\bullet}$ and aromatic amines, where the loss of isobutene arose from heterocleavage of the C–C bond linked to the – ^{t}Bu group on the *ortho* position.[56] Notably, we do not detect any H_2 but observe that more than one equivalent of ArOH is formed in the reaction suggesting that excess aryloxy radical serves as a hydrogen atom scavenger in the product forming step from **C-N$_{ortho}$** (Fig. 3). DFT investigation (B3PW91 functional, see ESI‡ for full computational details) of **3$_{Tol}$-NH$_2$** shows why it would prefer to engage in C–N coupling rather than undergo a second hydrogen atom abstraction. These computations show that the formally Fe(III)–NH_2 has significant unpaired spin density on N (22%) (Fig. 3) and has partial aminyl radical character.[57] Furthermore, the computed N–H BDE for **3$_{Tol}$-NH$_2$** is substantially higher (97.1 kcal mol^{-1}) than that of **1$_{Tol}$-NH$_3$**, indicating that a second abstraction is thermodynamically prohibited. Thus, amides **3$_{Ar}$-NH$_2$** react with the excess ArO$^{\bullet}$ *via* lower barrier, exothermic C–N heterocoupling of **3$_{Ar}$-NH$_2$** with the aromatic ring of ArO$^{\bullet}$ (Fig. 3). According to the calculations performed by Mayer and coworkers on the distribution of the residual spin density in ArO$^{\bullet}$, the *para* position contains the bulk of the unpaired density and is therefore the preferred site for reactivity.[58] However, here we observe no products arising from *para* heterocoupling in the reaction between **1$_{Ar}$-NH$_3$** and ArO$^{\bullet}$. By DFT computations, the C–N bond forming steps to intermediates **C-N$_{ortho}$** and **C-N$_{para}$** have a similar barrier of ~26 kcal mol^{-1}, but intermediate **C-N$_{ortho}$** is more stable than **C-N$_{para}$** by 10 kcal mol^{-1}; indeed, formation of the latter is endothermic, while the former is favorable by −4.2 kcal mol^{-1} (Fig. 3). This stabilization most likely arises from hydrogen bonding interaction similar to what is seen in the final product, which is absent in the intermediate produced from C–N bond formation at the *para* position. Assuming that loss of iso-butene is irreversible, the equilibrium between these two isomeric intermediates thus strongly favors the *ortho* species, leading to the observed products **2$_{Ar}$**.

The reaction pathway **C-N$_{ortho}$**, although unusual, complements the recent report by Bullock and coworkers using a Ru porphyrin system.[9] They proposed that a Ru(III)NH_2 intermediate, akin to complexes **3$_{Ar}$**, reacts with the *para* position of ArO$^{\bullet}$ to form a Ru(II)NH_2R complex, analogous to complex **C-N$_{para}$**. In their case, however, the Ru(II)–NH_2R bond is labile enough to release NH_2R in the presence of excess NH_3. Here, we do not observe any such turnover and **2$_{Ar}$** are terminal products in this reaction. The term "catalytic diversion" employed by Bullock can also be used here where the reactivity between ArO$^{\bullet}$ and **3$_{Ar}$-NH$_2$** prevents any catalysis to happen.

Iron amido complexes (Fe–NH_2) have been postulated as key intermediates in a variety of reactions.[22,59–61] In particular, Peters *et al.* recently reported a polypyridyl Fe catalyst for AO and proposed an Fe(III)NH_2 intermediate as part of their mechanistic analysis.[11] We therefore attempted to generate compound **3$_{Tol}$-NH$_2$** *via* other routes to obtain more direct evidence for it. Treatment of **1$_{Tol}$-NH$_3$** with other H atom abstractors like trityl radicals ($^{\bullet}$CPh$_3$ (ref. 62) or $^{\bullet}$C(*p*-^{t}Bu-Ph)$_3$ (ref. 63)) to prevent C–N coupling were unsuccessful, presumably due to steric effects. Therefore, two other paths (A and B, Scheme 4) to **3$_{Tol}$-NH$_2$** were explored.

Going from **1$_{Tol}$-NH$_3$** to **3$_{Tol}$-NH$_2$** can be seen as a proton-coupled electron transfer (PCET) by removal of a hydrogen

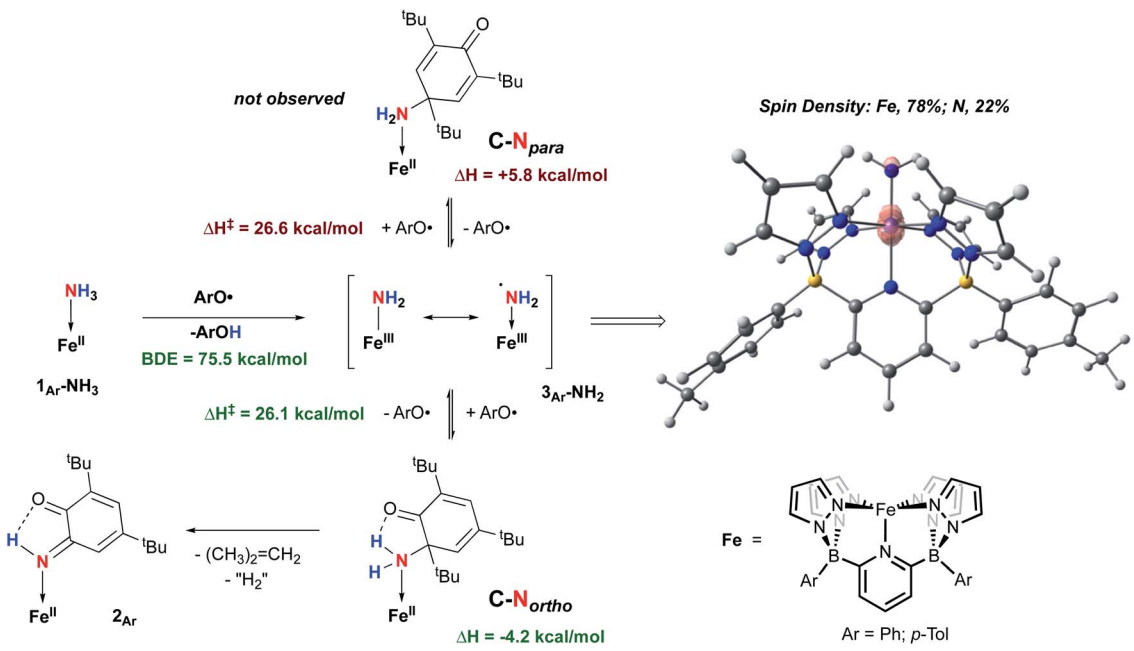

Fig. 3 Two mechanisms probed by DFT (B3PW91) calculation for the reactivity of **1$_{Ar}$-NH$_3$** and ArO$^{\bullet}$ at 298 K. Enthalpies are given relative to compound **1$_{Ar}$-NH$_3$** set to 0.0 kcal mol^{-1}.

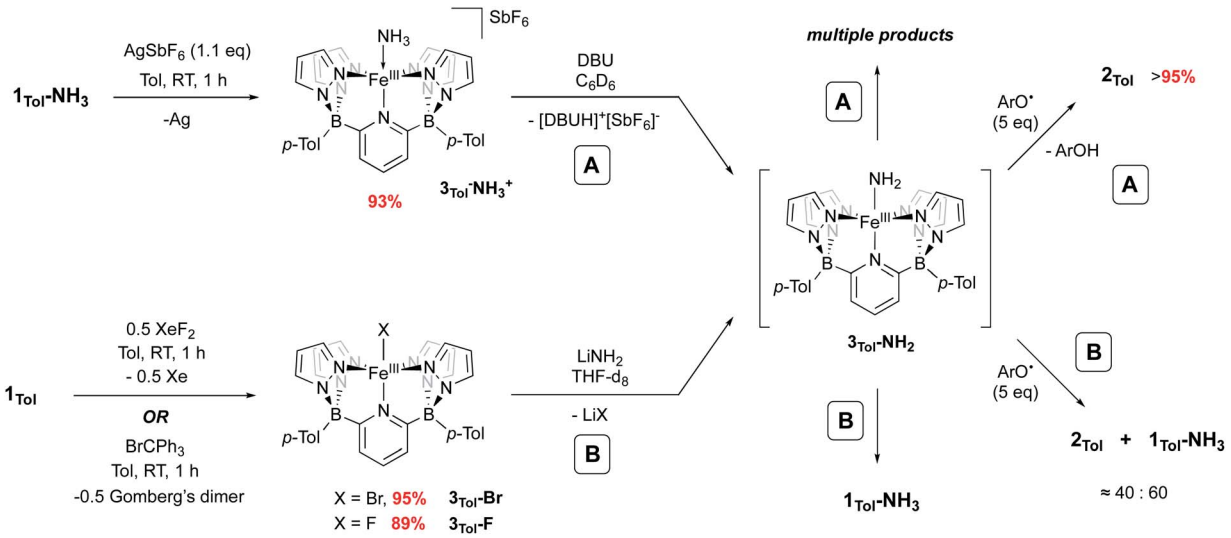

Scheme 4 Independent generation and trapping of 3_{Tol}-NH_2. (A) Oxidation of 1_{Tol}-NH_3 to 3_{Tol}-NH_3^+ and deprotonation with DBU. (B) Salt metathesis using 3_{Tol}-Br and 3_{Tol}-F.

atom ($H^•$) but can also be broken down into successive steps: oxidation by 1 e^- and removal of 1 H^+. **1_{Tol}-NH_3** is cleanly oxidized by $AgSbF_6$ in toluene, giving a dark red solution and deposited Ag(0). Upon work up, the Fe(III) ammine complex **3_{Tol}-NH_3^+** is isolated in excellent yield (93%, Scheme 4). **3_{Tol}-NH_3^+** exhibits a LS ($S = 1/2$) configuration ($\mu_{eff} = 1.80$ by Evans method), and its structure was confirmed by X-ray crystallography (Fig. 4). The shorter Fe–N10 bond of 2.010(2) in **3_{Tol}-NH_3^+** *vs.* 2.072(2) for **1_{Tol}-NH_3** confirmed the oxidation of the Fe center from +II to +III and is a rare example of a Fe–NH_3 adduct in the +III oxidation state.[64,65] The compound demonstrates the ability of the **B_2Pz_4Py** platform to stabilize and access higher oxidation state complexes. Deprotonation of **3_{Tol}-NH_3^+** with 1,8-diazabicyclo(5.4.0)undec-7-ene (DBU) was carried out at room temperature in C_6D_6. The reaction goes through a deep purple intermediate which rapidly turns into a gold coloured solution, which contains a mixture of paramagnetic species, including **1_{Tol}-NH_3** as the main product (Fig. S15 and S16‡). However, if the deprotonation of **3_{Tol}-$^{15}NH_3^+$** is performed in the presence of excess phenoxy radical ArO$^•$, the reaction proceeds cleanly and affords **2_{Tol}-^{15}N** as the sole iron-containing complex, along with ArOH and [DBUH][SbF_6] by-products (Fig. S17‡).

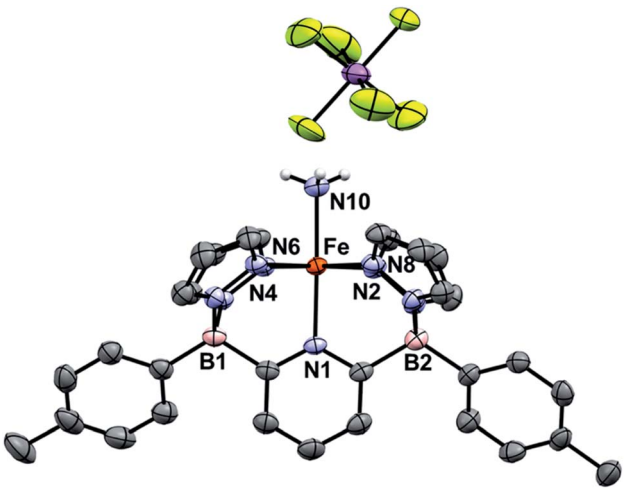

Fig. 4 ORTEP diagram for 3_{Tol}-NH_3^+. Hydrogen, boron, carbon, nitrogen, antimony, fluorine, and iron atoms are white, pink, grey, light blue, purple, yellow, and orange respectively. Thermal ellipsoids are shown at the 50% probability level. Calculated hydrogen atoms are omitted for clarity except those on the ammonia ligand (N10). The solvent molecule has been omitted for clarity. Selected bond distances (Å): Fe–N1, 2.009(3); Fe–N2, 1.999(4); Fe–N4, 1.990(3); Fe–N6, 1.951(3); Fe–N8, 1.942(4); Fe–N10, 2.010(3). Selected bond angles (°): N1–Fe–N2, 91.9(1); N2–Fe–N4, 94.7(1); N1–Fe–N10, 176.8(1). Further metrical data are given in Table S1.‡

Salt metathesis using $LiNH_2$ and an M–X (X = halogen) complex has been the most successful strategy employed to access and isolate M–NH_2 complexes.[43,44,66] We therefore attempted this reaction as depicted in Scheme 4, path B. The required Fe(III) halide complexes **3_{Tol}-X** (X = F, Br) were prepared by oxidation of **1_{Tol}** with XeF_2 or trityl bromide, respectively and were obtained in excellent yield. These compounds were fully characterized, including their solid state structures (Fig. S18,‡ **3_{Tol}-Br**; Fig. S19,‡ **3_{Tol}-F**). No reaction between these compounds and $LiNH_2$ was observed in non-polar solvents, even with addition of crown ethers, so THF-d_8 was employed. Perhaps unsurprisingly, when **3_{Tol}-Br** was treated with $LiNH_2$ in THF, after five days at RT, **1_{Tol}-NH_3** was isolated as the sole product of the reaction (Fig. S20 and S21‡). In this reaction, when **3_{Tol}-NH_2** is generated by salt metathesis, it acquires a hydrogen atom, most likely coming from the THF solvent[44,67] to form **1_{Tol}-NH_3**.[39] A similar result was observed when the iron fluoride **3_{Tol}-F** was employed, although the reaction was significantly faster. As with the deprotonation strategy, when these reactions were carried out in the presence of an excess of ArO$^•$, significant amounts of **2_{Tol}** were observed (up to ≈40%, Fig. S22 and S23‡), although here the scavenging of H atoms occurs at a competitive rate, with the balance of iron ending up as **1_{Tol}-NH_3**, as summarized in Scheme 4.

Taken together, the chemistry described above suggests that, while it is possible to generate $\mathbf{3_{Tol}}$-$\mathbf{NH_2}$ by a variety of methods, it is highly reactive due to a preponderance of spin density on the NH_2 nitrogen (Fig. 3). It thus behaves as an Fe(II) aminyl[57] and is readily trapped by ArO$^\bullet$ or scavenges H$^\bullet$ atoms from appropriate donors (THF coordinated to Li, for example). Our attempts to generate it in the absence of such traps were motivated by the possibility that it might dimerize through N–N bond formation, which has been proposed in a variety of catalytic cycles,[68] and in particular for ammonia oxidation catalysts operating through the hydrazine pathway (Scheme 1).[9,10] Indeed, such a process has recently been observed in a related d^7 Ni(III) system.[28] However, no evidence for this was found in any of the experiments used to generate $\mathbf{3_{Tol}}$-$\mathbf{NH_2}$. It occurred to us that, because of the electron rich nature of the $\mathbf{B_2Pz_4Py}$ ligand system, the Fe(II) compound might be a strong enough reductant to induce N–N bond cleavage in hydrazine, that is the reverse of homocoupling of $\mathbf{3_{Tol}}$-$\mathbf{NH_2}$. The reactions of $\mathbf{1_{Tol}}$ with hydrazine were thus explored and, as described below, a reaction path indicative of H_2N–NH_2 reductive cleavage is implicated by both experiments and computations.

When $\mathbf{1_{Tol}}$ is treated with 0.5 equivalents of hydrazine, a rapid color change from light green to dark forest green was observed and a clean ^{1}H NMR spectrum indicating the presence of two products was obtained (Fig. S24‡). One of the products is complex $\mathbf{1_{Tol}}$-$\mathbf{NH_3}$, which has already been made and characterized independently (Scheme 2 and Fig. 1). The second product, also diamagnetic, was isolated as a deep blue solid by washing the reaction mixture with cold Et_2O and was identified as described below to be the diazene dimer $\mathbf{4_{Tol}}$ (Scheme 5). When this reaction was carried out at −78 °C, ^{1}H NMR spectroscopy revealed that upon mixing $\mathbf{1_{Tol}}$ with hydrazine, an intermediate assigned as the dimeric hydrazine adduct $\mathbf{(1_{Tol})_2}$-$\mathbf{NH_2NH_2}$ is formed (Fig. S25‡). This intermediate is diamagnetic and the equivalent hydrazine protons appear at +3.65 ppm in the spectrum taken at 210 K, integrating to 4 relative to the 12 protons of the tolyl methyl groups and confirming its dimeric nature. This resonance appears as a broad doublet in a sample prepared with isotopically labeled $^{15}N_2H_4$, exhibiting a $^1J_{15N-1H}$ constant of 66 Hz (Fig. S26‡). As samples containing *in situ* generated $\mathbf{(1_{Tol})_2}$-$\mathbf{NH_2NH_2}$ are warmed to −15 °C, peaks corresponding to the two products $\mathbf{1_{Tol}}$-$\mathbf{NH_3}$ and $\mathbf{4_{Tol}}$ emerge with no

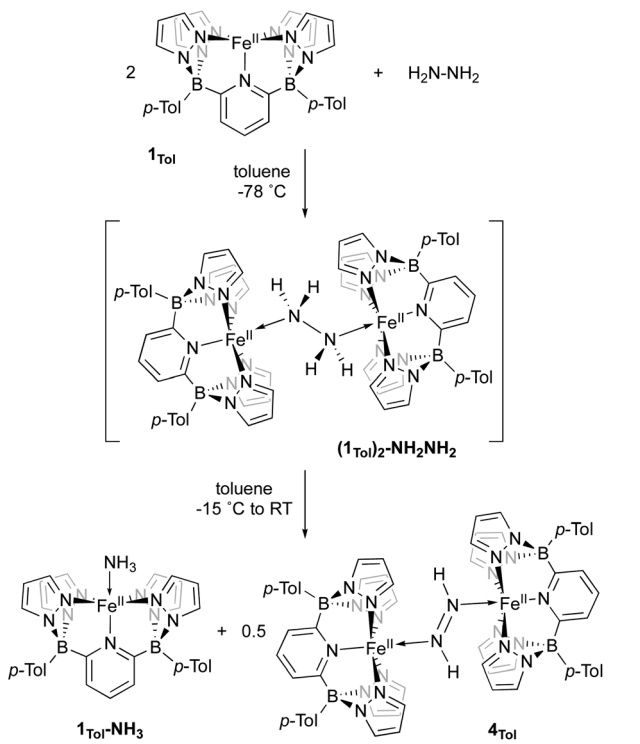

Scheme 5 The reaction of $\mathbf{1_{Tol}}$ with N_2H_4 and the two isolated products $\mathbf{1_{Tol}}$-$\mathbf{NH_3}$ and $\mathbf{4_{Tol}}$.

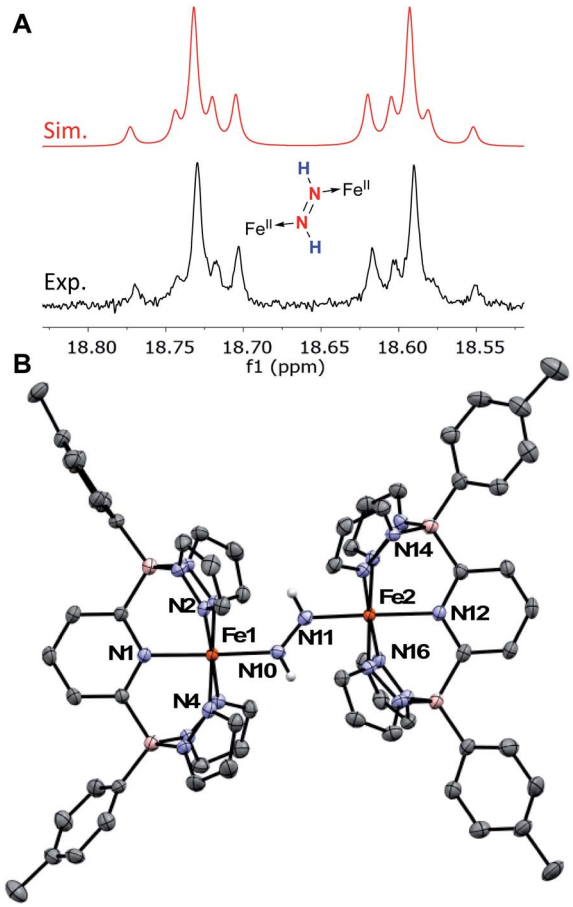

Fig. 5 (A) ^{1}H NMR spectra of the diazene multiplet of $\mathbf{4_{Tol}}$-$\mathbf{(^{15}N)_2}$ in C_6D_6 indicating an AA'XX' system (experimental, black; simulation, red). The experimental spectrum was simulated with TopSpin using the following parameters: $\delta = 18.66$ ppm; $^1J_{NH} = 69.4$ Hz; $^2J_{NH} = 0.45$ Hz; $^3J_{HH} = 22.4$ Hz (*trans*); $^1J_{NN} = 10.6$ Hz, and line width = 3.0 Hz. (B) ORTEP diagrams for $\mathbf{4_{Tol}}$. Thermal ellipsoids are shown at the 50% probability level. Calculated hydrogen atoms are omitted for clarity except those on the diazene ligand (N10 and N11). The molecule of solvent has been omitted for clarity. Selected bond distances (Å): Fe1–N1, 1.979(3); Fe1–N2, 2.001(3); Fe1–N4, 1.994(3); Fe1–N10, 1.923(3); Fe2–N11, 1.887(4); Fe2–N12, 2.031(4); Fe2–N14, 2.008(3); Fe2–N16, 2.026(2); N10–N11, 1.288(4). Selected bond angles (°): N2–Fe–N4, 91.9(1); N1–Fe–N10, 177.2(1); Fe1–N10–N11, 131.8(2); N14–Fe2–N16, 94.9(1); N12–Fe2–N11, 176.9(1); Fe2–N11–N10, 132.1(3). Further metrical data are given in Table S2.‡

other (diamagnetic) intermediates apparent (Fig. S27‡), until at room temperature the reaction proceeds to completion. Notably, no hydrogen gas was detected by ^{1}H NMR spectroscopy at any temperature during this experiment.

Complex $\mathbf{4_{Tol}}$ is a low spin, diamagnetic, Fe(II) complex and was characterized by a variety of spectroscopic techniques, as well as X-ray crystallography (Fig. 5). The diazene protons in the ^{1}H NMR spectrum appeared as a singlet at +18.66 ppm. When $^{15}N_2H_4$ is used, the singlet becomes a diagnostic AA'XX' multiplet (Fig. 5a), confirming the presence of a bridging diazene moiety. From the simulation of the multiplet (red spectrum, Fig. 5a), the different J values can be obtained.[55] In particular, the $^{3}J_{HH}$ of 22.4 Hz is consistent with a *trans* isomer, and in addition, a N–N bond length of 1.298 Å can be predicted based on the empirical correlation between the $^{3}J_{HH}$ value and the N–N bond distance of *trans* diazene complexes.[51,69] This is supported by the solid-state structure of $\mathbf{4_{Tol}}$ depicted in Fig. 5b. The N–N bond distance of 1.288(4) Å is consistent with an N–N double bond and with the predicted value, and the average value of 132° for the Fe–N=N bond angles is consistent with sp^2 hybridized nitrogen atoms. The shorter experimental N–N bond combined with the intense blue color of the species (Fig. S28‡) suggest a strong interaction between the Fe d orbitals and the π system of the diazene moiety. Furthermore, the rRaman spectrum of $\mathbf{4_{Tol}}$ shows an intense stretch at 1321 cm^{-1} corresponding to the $^{14}N{=}^{14}N$ bond. This band shifts to 1279 cm^{-1} for the $\mathbf{4_{Tol}}$-$(^{15}N)_2$ isotopologue, which is in good agreement with the calculated shift ($^{14N/15N}\Delta_{calc.} = 45$ cm^{-1}; $^{14N/15N}\Delta_{expt.} = 42$ cm^{-1}). Finally, the 80 K Mössbauer spectrum of $\mathbf{4_{Tol}}$ gives parameters $\delta = 0.41$ mm s^{-1} and $\Delta E_Q = 0.49$ mm s^{-1} which are in agreement with expectations for an Fe(II), LS complex (Fig. S29‡). Overall, the characteristics of complex $\mathbf{4_{Tol}}$ are similar to other Fe diazene complexes found in the literature but remains a rare example of a *trans* diazene Fe(II) complex.[51,70–72] Notably, complex $\mathbf{4_{Tol}}$ is highly thermally stable (heated at 110 °C in toluene for a week) and does not dissociate when subjected to vacuum (30 mTorr). This is reflective of the substitutionally inert low spin Fe(II) octahedral centre and attests to the robustness of Fe complexes supported by the $\mathbf{B_2Pz_4Py}$ ligand in comparison to other systems where the *trans* diazene complex is much more reactive.[51,73]

Even though the homogeneously catalysed disproportionation of hydrazine to ammonia and diazene has previously been reported in a few studies,[74–76] the mechanism of this transformation has yet to be studied in great detail.[60,68,77,78] We therefore sought to study the mechanism of the reaction between $\mathbf{1_{Tol}}$ and hydrazine, both experimentally and theoretically. Two main mechanisms are postulated to explain the formation of $\mathbf{1_{Tol}}$-$\mathbf{NH_3}$ and $\mathbf{4_{Tol}}$ from hydrazine disproportionation mediated by $\mathbf{1_{Tol}}$. They were probed by DFT calculations using the B3PW91 functional and are summarized in Fig. 6.

The coordination of hydrazine to $\mathbf{1_{Tol}}$ to form the hydrazine adduct $\mathbf{(1_{Tol})_2}$-$\mathbf{NH_2NH_2}$ is favored enthalpically by 40.0 kcal mol^{-1}, consistent with experimental observation.

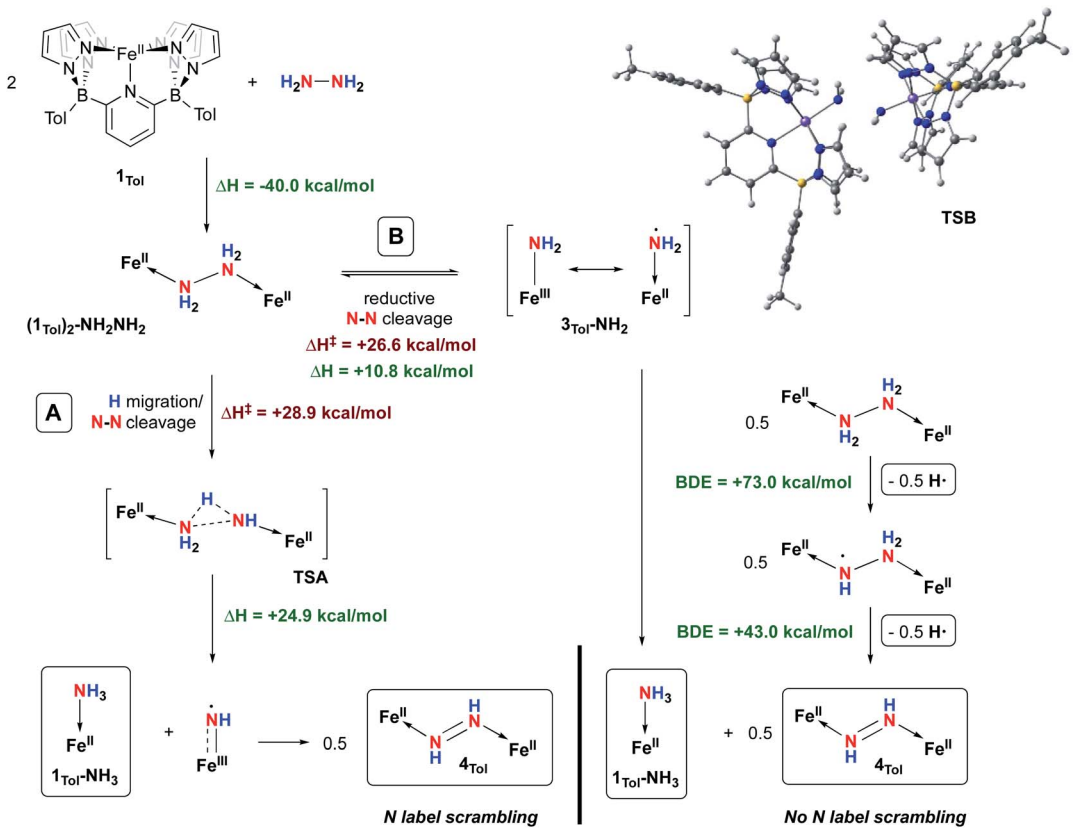

Fig. 6 Two potential mechanisms for the disproportionation of hydrazine using complex $\mathbf{1_{Tol}}$ at 298 K. Enthalpies are given relative to compound $\mathbf{1_{Tol}}$ set to 0.0 kcal mol^{-1}. The final products are shown in the boxes.

From this intermediate, two pathways for N–N bond cleavage can be envisioned. The first (path A) is reminiscent of what we proposed for O–O bond cleavage in the isoelectronic cobalt hydrogen peroxide dication, formed upon double protonation of the Co(III)–Co(III) peroxo complex supported by the $\mathbf{B_2Pz_4Py}$ framework.[37] Here, migration of a proton from one nitrogen to another is coupled with N–N cleavage in **TSA**, and this path leads directly to one of the observed products, $\mathbf{1_{Tol}\text{-}NH_3}$, along with the formally Fe(III) imidyl species shown with a barrier of 28.9 kcal mol^{-1}. This barrier is considerably higher than what we found for the same step in the $[Co(III)\text{–}(H)O\text{–}O(H)\text{–}Co(III)]^{2+}$ dication;[37] this is likely due to the lower acidity associated with the N–H protons in neutral $\mathbf{(1_{Tol})_2\text{-}NH_2NH_2}$. Furthermore, in contrast to the cobalt/hydrogen peroxide chemistry, the step through **TSA** is significantly endothermic (24.9 kcal mol^{-1}). However, computational analysis of the iron "imido" species shows that, like $\mathbf{3_{Tol}\text{-}NH_2}$, it is accurately described as an Fe(III) imidyl radical because the majority of spin density (54%) is found on the nitrogen as opposed to the iron (46%). This compound is therefore highly reactive and dimerizes in an exothermic reaction (more than 90 kcal mol^{-1}) to the observed diazene product $\mathbf{4_{Tol}}$, providing the main driving force for this path. It is likely that the *trans*-diazene is strongly favored for steric reasons, and we did not explore the path to formation of the *cis*-isomer. While some structurally characterized *cis*-diazene complexes exist,[79,80] they are favored by constraints imposed by the ligand systems employed and most adopt *trans* structures for both steric[51,70–72] and electronic[81,82] reasons.

The mechanism depicted in path A to the diazene product $\mathbf{4_{Tol}}$ should lead to scrambling of $^{14}N/^{15}N$ labeling if a mixture of $\mathbf{(1_{Tol})_2\text{-}^{14}NH_2{}^{14}NH_2}$ and $\mathbf{(1_{Tol})_2\text{-}^{15}NH_2{}^{15}NH_2}$ were allowed to proceed to formation of the products. The isotopic distribution within the N=N bond in the product $\mathbf{4_{Tol}}$ can be determined by rRaman spectroscopy. The reaction of $\mathbf{1_{Tol}}$ with a 1 : 1 mixture of $^{15}N_2H_4$ and $^{14}N_2H_4$ at 210 K as described above generates the required 1 : 1 mixture of isotopologues. As shown in Fig. 7, analysis of the rRaman spectrum of the product mixture clearly shows that only unscrambled $\mathbf{4_{Tol}\text{-}(^{14}N)_2}$ and $\mathbf{4_{Tol}\text{-}(^{15}N)_2}$ were formed, with no evidence of the mixed isotopologue $\mathbf{4_{Tol}\text{-}^{14}N\text{–}^{15}N}$. This experiment prompted us to consider a mechanism in which isotopic scrambling would not be predicted, namely path B in Fig. 6.

Pathway B is based on an equilibrium between the hydrazine adduct $\mathbf{(1_{Tol})_2\text{-}NH_2NH_2}$ and its monomeric form, complex $\mathbf{3_{Tol}\text{-}NH_2}$ (Fig. 6). Computational analysis of this step reveals that it is endothermic by 10.8 kcal mol^{-1}, but proceeds *via* **TSB**, which is lower in energy than **TSA** by 2.3 kcal mol^{-1}. The N–N distance in **TSB** is 2.332 Å, indicating that most of the barrier is due to homolytic cleavage of the N–N bond in coordinated hydrazine. While dimerization back to $\mathbf{(1_{Tol})_2\text{-}NH_2NH_2}$ has a low barrier ($\approx$15 kcal mol^{-1}), if $\mathbf{3_{Tol}\text{-}NH_2}$ finds another equivalent of $\mathbf{(1_{Tol})_2\text{-}NH_2NH_2}$ it may abstract a relatively weak N–H bond (73.0 kcal mol^{-1}, *cf.* that of 75.5 kcal mol^{-1} in $\mathbf{1_{Tol}\text{-}NH_3}$). The resulting complex has an even weaker N–H bond of 43.0 kcal mol^{-1}, and undergoes further H atom abstraction to yield the diazene product $\mathbf{4_{Tol}}$. This path is consistent with the lack of scrambling of nitrogen label in the experiment described above. Because of the endothermic nature of equilibrium of path B, the concentration of highly reactive $\mathbf{3_{Tol}\text{-}NH_2}$ is expected to be very small and would scavenge an H atom from the weakest and most abundant source in the medium, in this case $\mathbf{(1_{Tol})_2\text{-}NH_2NH_2}$. Unfortunately, attempts to detect the LS ($S = 1/2$) iron amido/amidyl species $\mathbf{3_{Tol}\text{-}NH_2}$ by following the reaction of $\mathbf{1_{Tol}}$ with hydrazine by low temperature EPR spectroscopy were not successful, indicating it must be an extremely short-lived species.

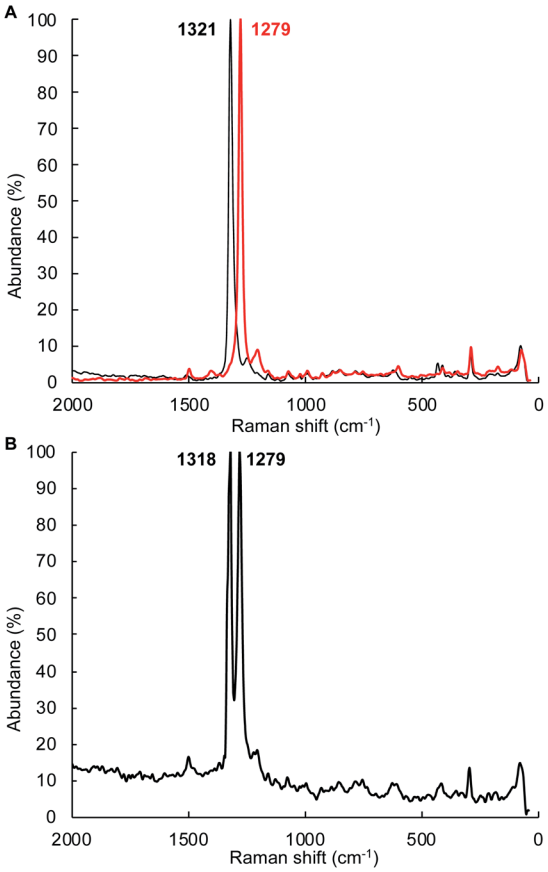

Fig. 7 Scrambling of ^{n}N label in the disproportionation of a 1 : 1 mixture of $^{15}N_2H_4$ and $^{14}N_2H_4$ with $\mathbf{1_{Tol}}$ as determined by resonance Raman spectroscopy. The rRaman spectra were obtained with a 1064 nm laser excitation wavelength at room temperature. A. rRaman spectra of $\mathbf{4_{Tol}\text{-}(^{14}N)_2}$ (black trace) and $\mathbf{4_{Tol}\text{-}(^{15}N)_2}$ (red trace). (B) rRaman spectrum of the $\mathbf{4_{Tol}\text{-}(^{n}N)_2}$ isotopologues obtained by reaction of $^{n}N_2H_4$ with $\mathbf{1_{Tol}}$.

Conclusions

Iron(II) complexes supported by the dianionic, pentadentate ligand platform $\mathbf{B_2Pz_4Py}$[39] were used to coordinate and activate ammonia and hydrazine. Several lines of experimental evidence, supported by DFT computations, implicate the generation of a highly reactive aminyl species, $\mathbf{3_{Ar}\text{-}NH_2}$ through abstraction of $H^{\bullet}$ or H^{+} from suitable precursors. Such compounds are understood to be important intermediates in ammonia oxidation processes as mediated by transition metal-based catalysts. While $\mathbf{3_{Ar}\text{-}NH_2}$ might formally be regarded as an

Fe(III) amido derivative, the electron richness of the diborate ligand framework favors the Fe(II) aminyl formulation, accounting for its high propensity to react with other radical species (*e.g.* ArO$^{\bullet}$) or H$^{\bullet}$ sources. Interestingly, this compound also appears to be accessible *via* hydrazine activation through a reductive cleavage of the N–N bond in hydrazine. This is the reverse of a potentially important N–N bond forming path in AO. These transformations show that the tetrapodal pentadentate platform furnished by the **B_2Pz_4Py** ligand has promise not only for studying new stoichiometric reactions of archetypical nitrogen containing fuel sources, but also for catalyst development.

Conflicts of interest

There are no conflicts to declare.

Acknowledgements

W. E. P. thanks the Canada Research Chair secretariat for a Tier I CRC (2013–2027). Funding for the experimental work described was provided by the Natural Sciences and Engineering Research Council of Canada in the form of a Discovery Grant to W. E. P. Funding for the computational work described was provided by a French CNRS PICS project. L. N. thanks Alberta Innovates Technology Futures and the Vanier Canada Graduate Scholarships for support. LM is a senior member of the Institut Universitaire de France. Y. Y. thanks the Chinese Scholarship Council (CSC) for financial support. CalMip is acknowledged for a generous grant of computing time. M. L. N. acknowledges support for this work from the National Institutes of Health under grant R01GM111480.

Notes and references

1 N. S. Lewis and D. G. Nocera, *Proc. Natl. Acad. Sci. U. S. A.*, 2006, **103**, 15729–15735.
2 H. B. Gray, *Nat. Chem.*, 2009, **1**, 7.
3 J. G. Chen, R. M. Crooks, L. C. Seefeldt, K. L. Bren, R. M. Bullock, M. Y. Darensbourg, P. L. Holland, B. Hoffman, M. J. Janik, A. K. Jones, M. G. Kanatzidis, P. King, K. M. Lancaster, V. S. Lymar, P. Pfromm, W. F. Schneider and R. R. Schrock, *Science*, 2018, **360**, eaar6611.
4 P. H. Pfromm, *J. Renewable Sustainable Energy*, 2017, **9**, 034702.
5 G. Soloveichik, *Nat. Catal.*, 2019, **2**, 377–380.
6 N. M. Adli, H. Zhang, S. Mukherjee and G. Wu, *J. Electrochem. Soc.*, 2018, **165**, 3130–3147.
7 S. T. Hatscher, T. Fetzer, E. Wagner and H.-J. Kneuper, in *Handbook of Heterogeneous Catalysis*, 2008, pp. 2575–2592, DOI: 10.1002/9783527610044.hetcat0130.
8 P. Bhattacharya, Z. M. Heiden, G. M. Chambers, S. I. Johnson, R. M. Bullock and M. T. Mock, *Angew. Chem., Int. Ed.*, 2019, **58**, 11618–11624.
9 P. L. Dunn, S. I. Johnson, W. Kaminsky and R. M. Bullock, *J. Am. Chem. Soc.*, 2020, **142**, 3361–3365.
10 F. Habibzadeh, S. L. Miller, T. W. Hamann and M. R. Smith, *Proc. Natl. Acad. Sci. U. S. A.*, 2019, **116**, 2849–2853.
11 M. D. Zott, P. Garrido-Barros and J. C. Peters, *ACS Catal.*, 2019, **9**, 10101–10108.
12 K. Nakajima, H. Toda, K. Sakata and Y. Nishibayashi, *Nat. Chem.*, 2019, **11**, 702–709.
13 P. L. Dunn, B. J. Cook, S. I. Johnson, A. M. Appel and R. M. Bullock, *J. Am. Chem. Soc.*, 2020, **142**, 17845–17858.
14 J. J. Warren, T. A. Tronic and J. M. Mayer, *Chem. Rev.*, 2010, **110**, 6961–7001.
15 D. Cheddie, in *Hydrogen Energy – Challenges and Perspectives*, 2012, DOI: 10.5772/47759.
16 J. Zhao, *Science*, 2005, **307**, 1080–1082.
17 V. D. Gutsulyak, W. E. Piers, J. Borau-Garcia and M. Parvez, *J. Am. Chem. Soc.*, 2013, **135**, 11776–11779.
18 G. W. Margulieux, Z. R. Turner and P. J. Chirik, *Angew. Chem., Int. Ed.*, 2014, **53**, 14211–14215.
19 E. Khaskin, M. A. Iron, L. J. W. Shimon, J. Zhang and D. Milstein, *J. Am. Chem. Soc.*, 2010, **132**, 8542–8543.
20 Y.-H. Chang, Y. Nakajima, H. Tanaka, K. Yoshizawa and F. Ozawa, *J. Am. Chem. Soc.*, 2013, **135**, 11791–11794.
21 R. M. Brown, J. Borau-Garcia, J. Valjus, C. J. Roberts, H. M. Tuononen, M. Parvez and R. Roesler, *Angew. Chem., Int. Ed.*, 2015, **54**, 6274–6277.
22 M. G. Scheibel, J. Abbenseth, M. Kinauer, F. W. Heinemann, C. Würtele, B. De Bruin and S. Schneider, *Inorg. Chem.*, 2015, **54**, 9290–9302.
23 M. J. Bezdek, S. Guo and P. J. Chirik, *Science*, 2016, **354**, 730–733.
24 G. W. Margulieux, M. J. Bezdek, Z. R. Turner and P. J. Chirik, *J. Am. Chem. Soc.*, 2017, **139**, 6110–6113.
25 M. J. Bezdek and P. J. Chirik, *Angew. Chem., Int. Ed.*, 2018, **130**, 2246–2250.
26 P. Bhattacharya, Z. M. Heiden, E. S. Wiedner, S. Raugei, N. A. Piro, W. S. Kassel, R. M. Bullock and M. T. Mock, *J. Am. Chem. Soc.*, 2017, **139**, 2916–2919.
27 B. J. Cook, S. I. Johnson, G. M. Chambers, W. Kaminsky and R. M. Bullock, *Chem. Commun.*, 2019, **55**, 14058–14061.
28 G. Nina, O. H. Paul and P. Jonas, *Hydrazine Formation via NiIII-NH2 Radical Coupling in Ni-Mediated Ammonia Oxidation*, 2020.
29 J. Y. Shen, M. Wang, P. L. Zhang, J. Jiang and L. C. Sun, *Chem. Commun.*, 2017, **53**, 4374–4377.
30 D. J. Wasylenko, R. D. Palmer and C. P. Berlinguette, *Chem. Commun.*, 2013, **49**, 218–227.
31 D. M. Ekanayake, K. M. Kulesa, J. Singh, K. K. Kpogo, S. Mazumder, H. B. Schlegel, C. N. Verani, H. Bernhard Schlegel and C. N. Verani, *Dalton Trans.*, 2017, **46**, 16812–16820.
32 W. T. Eckenhoff, *Coord. Chem. Rev.*, 2018, **373**, 295–316.
33 L. Z. Chen, A. Khadivi, M. Singh and J. W. Jurss, *Inorg. Chem. Front.*, 2017, **4**, 1649–1653.
34 R. T. Jonas and T. D. P. Stack, *J. Am. Chem. Soc.*, 1997, **119**, 8566–8567.
35 M. E. de Vries, R. M. La Crois, G. Roelfes, H. Kooijman, A. L. Spek, R. Hage and B. L. Feringa, *Chem. Commun.*, 1997, 1549–1550.

36 S. I. Johnson, S. P. Heins, C. M. Klug, E. S. Wiedner, R. M. Bullock and S. Raugei, *Chem. Commun.*, 2019, **55**, 5083–5086.
37 L. Nurdin, D. M. Spasyuk, L. Fairburn, W. E. Piers and L. Maron, *J. Am. Chem. Soc.*, 2018, **140**, 16094–16105.
38 D. W. Beh, W. E. Piers, B. S. Gelfand and J.-B. Lin, *Dalton Trans.*, 2020, **49**, 95–101.
39 D. M. Spasyuk, S. H. Carpenter, C. E. Kefalidis, W. E. Piers, M. L. Neidig and L. Maron, *Chem. Sci.*, 2016, **7**, 5939–5944.
40 D. W. Beh, W. E. Piers, I. del Rosal, L. Maron, B. S. Gelfand, C. Gendy and J.-B. Lin, *Dalton Trans.*, 2018, **47**, 13680–13688.
41 L. Nurdin, D. M. Spasyuk, W. E. Piers and L. Maron, *Inorg. Chem.*, 2017, **56**, 4157–4168.
42 T. J. Morin, B. Bennett, V. S. Lindeman and J. R. Gardinier, *Inorg. Chem.*, 2008, **47**, 7468–7470.
43 D. J. Fox and R. G. Bergman, *J. Am. Chem. Soc.*, 2003, **125**, 8984–8985.
44 S. E. Creutz and J. C. Peters, *Chem. Sci.*, 2017, **8**, 2321–2328.
45 J. S. Anderson, M.-E. Moret and J. C. Peters, *J. Am. Chem. Soc.*, 2013, **135**, 534–537.
46 J. J. Kiernicki, E. E. Norwine, M. Zeller and N. K. Szymczak, *Chem. Commun.*, 2019, **55**, 11896–11899.
47 A. J. Mountford, W. Clegg, S. J. Coles, R. W. Harrington, P. N. Horton, S. M. Humphrey, M. B. Hursthouse, J. A. Wright and S. J. Lancaster, *Chem.–Eur. J.*, 2007, **13**, 4535–4547.
48 R. A. Andersen, K. Faegri, J. C. Green, A. Haaland, M. F. Lappert, W. P. Leung and K. Rypdal, *Inorg. Chem.*, 1988, **27**, 1782–1786.
49 D. L. J. Broere, I. Čorić, A. Brosnahan and P. L. Holland, *Inorg. Chem.*, 2017, **56**, 3140–3143.
50 L. Nurdin, Ph.D. thesis, University of Calgary, 2020.
51 C. T. Saouma, C. E. Moore, A. L. Rheingold and J. C. Peters, *Inorg. Chem.*, 2011, **50**, 11285–11287.
52 Y. Lee, N. P. Mankad and J. C. Peters, *Nat. Chem.*, 2010, **2**, 558–565.
53 D. N. Bowman and E. Jakubikova, *Inorg. Chem.*, 2012, **51**, 6011–6019.
54 Y. Shimura, *Bull. Chem. Soc. Jpn.*, 1988, **61**, 693–698.
55 J. Mason, in *Patai's Chemistry of Functional Groups*, 2009, DOI: 10.1002/9780470682531.pat0148.
56 M. Hedoyatullah and F. Thevenet, *Bull. Soc. Chim. Belg.*, 2010, **96**, 311–323.
57 A. I. O. Suarez, V. Lyaskovskyy, J. N. H. Reek, J. I. van der Vlugt, B. de Bruin, J. I. van der Vlugt and B. de Bruin, *Angew. Chem., Int. Ed.*, 2013, **52**, 12510–12529.
58 V. W. Manner, T. F. Markle, J. H. Freudenthal, J. P. Roth and J. M. Mayer, *Chem. Commun.*, 2008, 256–258.
59 R. L. Lucas, D. R. Powell and A. S. Borovik, *J. Am. Chem. Soc.*, 2005, **127**, 11596–11597.
60 K. Umehara, S. Kuwata and T. Ikariya, *J. Am. Chem. Soc.*, 2013, **135**, 6754–6757.
61 Y.-H. Chang, P.-M. Chan, Y.-F. Tsai, G.-H. Lee and H.-F. Hsu, *Inorg. Chem.*, 2014, **53**, 664–666.
62 M. Gomberg, *J. Am. Chem. Soc.*, 1900, **22**, 757–771.
63 T. H. Colle and E. S. Lewis, *J. Am. Chem. Soc.*, 1979, **101**, 1810–1814.
64 N. S. Sickerman, S. M. Peterson, J. W. Ziller and A. S. Borovik, *Chem. Commun.*, 2014, **50**, 2515–2517.
65 M. M. Olmstead, G. Sigel, H. Hope, X. Xu and P. P. Power, *J. Am. Chem. Soc.*, 1985, **107**, 8087–8091.
66 J. S. Anderson, J. Rittle and J. C. Peters, *Nature*, 2013, **501**, 84–87.
67 G. T. Sazama and T. A. Betley, *Inorg. Chem.*, 2010, **49**, 2512–2524.
68 C. Ferousi, S. H. Majer, I. M. DiMucci and K. M. Lancaster, *Chem. Rev.*, 2020, **120**, 5252–5307.
69 M. A. Cooper and S. L. Manatt, *J. Am. Chem. Soc.*, 1969, **91**, 6325–6333.
70 D. Sellmann and J. Sutter, *Acc. Chem. Res.*, 1997, **30**, 460–469.
71 D. Sellmann, W. Soglowek, F. Knoch and M. Moll, *Angew. Chem., Int. Ed.*, 1989, **28**, 1271–1272.
72 D. Sellmann, D. C. F. Blum and F. W. Heinemann, *Inorg. Chim. Acta*, 2002, **337**, 1–10.
73 C. G. Balesdent, J. L. Crossland, D. T. Regan, C. T. López and D. R. Tyler, *Inorg. Chem.*, 2013, **52**, 14178–14187.
74 N. X. Gu, G. Ung and J. C. Peters, *Chem. Commun.*, 2019, **55**, 5363–5366.
75 P. B. Hitchcock, D. L. Hughes, M. J. Maguire, K. Marjani and R. L. Richards, *J. Chem. Soc., Dalton Trans.*, 1997, **24**, 4747–4752.
76 L. D. Field, H. L. Li and A. M. Magill, *Inorg. Chem.*, 2009, **48**, 5–7.
77 H. Tanaka, S. Hitaoka, K. Umehara, K. Yoshizawa and S. Kuwata, *Eur. J. Inorg. Chem.*, 2020, **2020**, 1472–1482.
78 Y. Zheng, W. Zheng, J. Wang, H. Chang and D. Zhu, *J. Phys. Chem. A*, 2018, **122**, 2764–2780.
79 Y. Chen, L. Liu, Y. Peng, P. Chen, Y. Luo and J. Qu, *J. Am. Chem. Soc.*, 2011, **133**, 1147–1149.
80 C. T. Saouma, P. Müller and J. C. Peters, *J. Am. Chem. Soc.*, 2009, **131**, 10358–10359.
81 J. A. Pople and L. A. Curtiss, *J. Chem. Phys.*, 1991, **95**, 4385–4388.
82 A. Sindhu, R. Pradhan, U. Lourderaj and M. Paranjothy, *Phys. Chem. Chem. Phys.*, 2019, **21**, 15678–15685.